










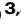





Van der Waals photonic integrated circuit with coherent light generation

Received: 16 March 2025

Accepted: 3 June 2025

Published online: 01 July 2025

 Check for updates

Tianhua Ren ^{1,2,3,4,11}, Andrés Granados del Águila ^{5,11} ,
Zhaolong Chen ^{3,4,6,11}, Qianhui Xu ², Xuehong Zhou², Rui Duan ^{1,2},
Magdalena Grzeszczyk³, Xiao Gong ^{4,7}, Kenji Watanabe ⁸,
Takashi Taniguchi ⁹, Kostya S. Novoselov ^{3,4} , Maciej Koperski ^{3,10}  &
Handong Sun ¹ 

Two-dimensional semiconductors hold great potential as coherent light sources for photonic integrated circuits. However, the conventional integration of two-dimensional materials onto silicon photonics introduces significant structural and optoelectronic drawbacks, hindering the practical realization of coherent photonic circuits. Here, we introduce the concept of a van der Waals photonic integrated circuit, which is a complete on-chip optical system fabricated entirely from a van der Waals heterostructure. By combining multifunctional two-dimensional materials into a single heterostructure, we realize a fully functional photonic circuitry capable of benchtop coherent light generation, propagation, transmission, and modulation via a silicon back gate. The monolithic approach to heterostructure circuitry supports the effective integration of various photonic components based on two-dimensional materials with stable electro-optic interconnections. The coherence of light emission is systematically verified by second-order correlation experiments at room temperature, showing a clear power-dependent transition to a Poissonian regime. Our work establishes a pathway for coherent van der Waals photonics incorporated with standard silicon manufacturing processes.

Coherent light sources (CLS) constitute the essential building blocks providing coherent photons in silicon-based photonic integrated circuits (PICs)^{1–4}. Multiple applications rely on compact and on-chip integrated CLSs, including the generation of high-dimensional orbital angular momentum states of light⁵, high-speed electro-optical interconnections⁶, and optical computing based on neural network⁷.

The inherent indirect band gap of silicon prevents the realization of silicon-based CLSs. Consequently, it is essential to develop on-chip optical gain media for the CLSs that are compatible with silicon technology. Well-studied examples of silicon-integrated gain media include hybrid bonding⁸, micro-printing⁹, and epitaxial growth^{10,11} of direct-bandgap III-V semiconductors or GeSn, and implantation of

¹Institute of Applied Physics and Materials Engineering, University of Macau, Macau, China. ²Division of Physics and Applied Physics, School of Physical and Mathematical Sciences, Nanyang Technological University, Singapore, Singapore. ³Institute for Functional Intelligent Materials, National University of Singapore, Singapore, Singapore. ⁴Centre for Advanced 2D Materials, National University of Singapore, Singapore, Singapore. ⁵Institute of Materials Science (ICMUV), University of Valencia, Valencia, Spain. ⁶School of Advanced Materials, Peking University Shenzhen Graduate School, Shenzhen, China. ⁷Department of Electrical and Computer Engineering, National University of Singapore, Singapore, Singapore. ⁸Research Center for Electronic and Optical Materials, National Institute for Materials Science, Tsukuba, Japan. ⁹Research Center for Materials Nanoarchitectonics, National Institute for Materials Science, Tsukuba, Japan. ¹⁰Department of Materials Science and Engineering, National University of Singapore, Singapore, Singapore. ¹¹These authors contributed equally: Tianhua Ren, Andrés Granados del Águila, Zhaolong Chen. ✉ e-mail: andres.granados@uv.es; kostya@nus.edu.sg; msemaci@nus.edu.sg; hdsun@um.edu.mo

ions¹. However, such advances are incompatible with standard silicon processes or cannot reach the benchtop performance of off-chip CLSs. Over the last two decades, the emerging two-dimensional (2D) transition metal dichalcogenides (TMDs) have become a promising on-chip gain media due to their direct bandgap^{12,13} and tightly bound exciton at room temperature^{14–16} of monolayer TMDs with strong excitonic gain below the Mott transition¹⁷. The unique van der Waals (vdW) structure¹⁸ of TMDs holds great potential to achieve practical 2D-silicon integration with high quality and low cost¹⁹, while removing the requirement of lattice matching in creating photonic circuits. Various 2D-TMD-based lasers have been reported^{20–27}, whose lasing actions were found with typical quality factor below 1000 and various power density thresholds from 1 to 10^4 W cm⁻² under continuous-wave (CW) pumping (Supplementary Table S1).

2D-based CLSs are still at an early stage of development. Besides the demonstrations of lasing action with coherent emission, 2D materials are limited for direct and flexible integration with silicon photonics. Current 2D-based lasers rely predominantly on transferring 2D materials onto the surfaces of external cavities^{20,22–24,26}, whose structures suffer from significant defects²⁸, unintentional doping²⁹, and optical losses³⁰. Furthermore, the rudimentary fabrication of lasing structures hinders the realization of stable metallic contacts required for electrical pumping and modulation, thus impeding the demonstration of practical prototype devices with electrical modulation and injection.

In this work, we address these challenges by introducing a new architecture of vdW PIC based on a single monolithic vdW heterostructure, where coherent light is generated, propagated, and

modulated within a compact chip-based photonic circuitry. This vdW PIC is a compelling solution for on-chip coherence that is compatible with silicon technology. The vdW PIC comprises a vdW heterostructure with an atomically precise assembly of monolayer TMD of WS₂ as an optical gain medium sandwiched by optical confining structures based on hexagonal boron nitride (hBN). Importantly, the van der Waals structure was monolithically patterned into a CLS with a high quality factor (Q) of 2500, conserving the same optical confinement of suspended cavities²¹ while directly integrated on the surface of a silicon chip. Its light-confining characteristics enable the realization of the CLS exhibiting a low coherence threshold of ~ 10 W cm⁻² under CW pumping at room temperature, with its coherence confirmed through a systematic examination of second-order photon correlation experiments. We further integrated such CLSs into a vdW PIC by fabricating an entire vdW heterostructure into interconnected photonic components, including hBN waveguides, free-beam grating couplers, and graphene-based electrical modulators of emission intensity. This prototype constates complete and fully functional PICs readily compatible with matured silicon photonics and other arbitrary substrates. Our vdW PICs could serve as building blocks for the next-generation coherent photonic chips, while their universal design is conducive to the practical CLS with electrical injections. Given the progress in the fabrication of wafer scale vdW heterostructures^{31–34}, our results could be scaled up to become relevant for practical applications.

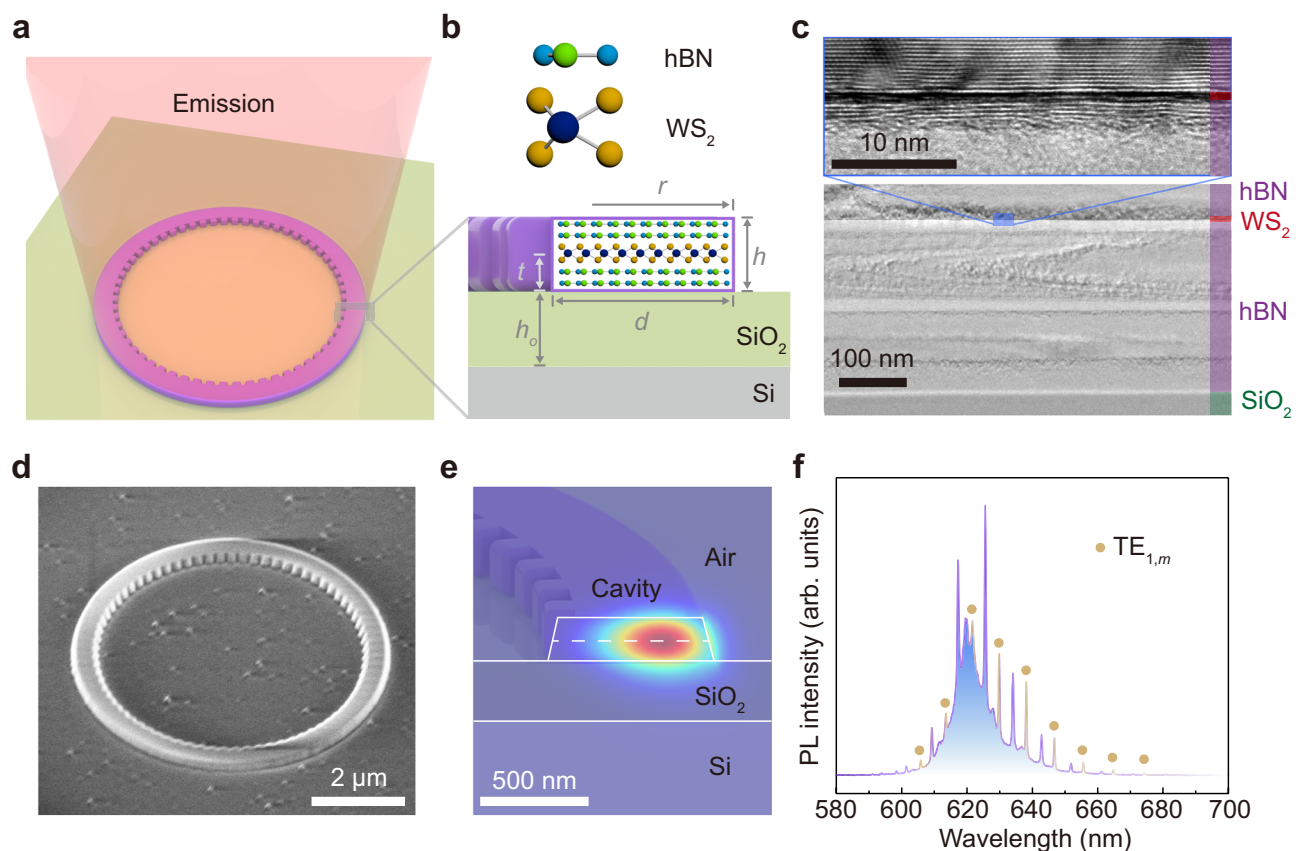


Fig. 1 | Design of vdW heterostructure cavity. **a** Schematic of ring-shaped heterostructure cavity on silicon oxide/silicon substrate. **b** Cross-sectional illustration of on-chip integration. Structural parameters of r , h , d , and h_o are ring radius, height, width, and silicon oxide thickness, respectively. **c** Cross-sectional bright-field transmission electron microscopy (TEM) image of vdW heterostructure with inset of zoomed-in high-resolution TEM image of the blue region. False colours indicate the

different materials forming the vdW heterostructure. **d** Scanning electron microscopy (SEM) image of cavity. **e** Cross-sectional view of the axis-symmetrically simulated electric-field profiles of first-order transverse electric (TE₁) whispering-gallery modes (WGMs). White dashed line denotes the WS₂ position. **f** Photoluminescence spectrum for ring cavity with multiple TE₁ WGMs highlighted by yellow dots. The second-order TE₂ modes are spectrally located between TE₁ modes.

Results

Van der Waals coherent light source

The architecture of the vdW CLS in the form of a hBN/WS₂/hBN ring cavity on Si/SiO₂ substrate is schematically illustrated in Fig. 1a, b. In this vdW heterostructure, a monolayer WS₂ serves as the optical gain material, while the dielectric hBN layers provide encapsulation, enabling atomically smooth interfaces and optical confinement. This cavity was fabricated by dry transfer of films mechanically exfoliated from single crystals and stacked vertically to form a heterostructure, followed by a monolithic nano-patterning process into a ring cavity³⁵. The top and bottom hBN films of 100 nm thickness each act as dielectric layers exhibiting a high refractive index (~ 2.1 ^{36,37}), which ensures excellent optical confinement^{35,36,38,39}. The SiO₂ layer with a thickness of 285 nm or 1000 nm isolates the optical absorption from the silicon substrate underneath. The WS₂ monolayer was placed at the spatial maximum of the optical mode, by which coupling strength to cavity modes is optimized^{35,40}.

The vdW CLS was characterized by scanning transmission electron microscopy (TEM) (Fig. 1c) and scanning electron microscopy (SEM) (Fig. 1d). Our TEM and SEM characterizations demonstrate the uniform layered structure and ultra-smooth interfaces of WS₂/hBN and hBN/SiO₂. The vdW assembly-induced defects, such as bubbles or wrinkles, were absent in the entire cavity, as illustrated by TEM. The lattice mismatch between WS₂ and hBN results in a strain of up to 0.08%⁴¹, which is usually relaxed by forming nano- to micro-sized bubbles along the out-of-plane direction⁴². Our cavity architecture was designed to address this challenge by employing 100 nm thick hBN films to form the heterostructure, where interfacial strain is allowed to

gradually relax along the out-of-plane direction away from the TMD monolayer. This strategy follows the methodology of buffer layers in the epitaxial growth of III-V¹⁰ or GeSn¹¹ hetero-epitaxy on silicon. Moreover, the hBN encapsulation provides air-tight protection⁴³ of the gain medium, defect passivation⁴⁴, and self-cleaning⁴⁵, resulting in long-range ultra-smooth interfaces enabling a robust light-emitting system suitable for PIC integrations. Importantly, the quantum yield of WS₂ with hBN encapsulation was found to be $\sim 20\%$ for the entire pumping power range in our measurements at room temperature, which is a few orders higher than quantum yield in the previous work of WS₂-based laser²¹, showing the potential as robust gain media for CLS demonstrations (Supplementary Fig. S4).

We design the ring cavity with radius r of 3.5 μm and width d of 800 nm on the SiO₂/Si substrate with SiO₂ thickness h_o of 285 nm. The cavity thickness h is ~ 200 nm, consisting of two identically 100 nm thick hBN and a monolayer WS₂. The WS₂ monolayer covers the entire cavity area. The ultra-smooth surface of vdW heterostructure prevents any detectable scattering of the cavity mode. Therefore, gratings are introduced on the inner wall of the ring to direct a portion of the cavity emission vertically for the convenience of confocal photoluminescence (PL) measurements. Our finite element simulations show that transverse electric (TE)-polarized whispering gallery modes (WGMs) are supported by the cavity and that they can couple to excitons^{20,21,35,40} (Fig. 1e). The optical structures based on vdW heterostructure are patterned by following standard silicon process, including electron beam lithography and reactive ion etching. We characterize the cavity emission using PL measurements under a confocal microscope pumped by a 532 nm CW laser excitation at room

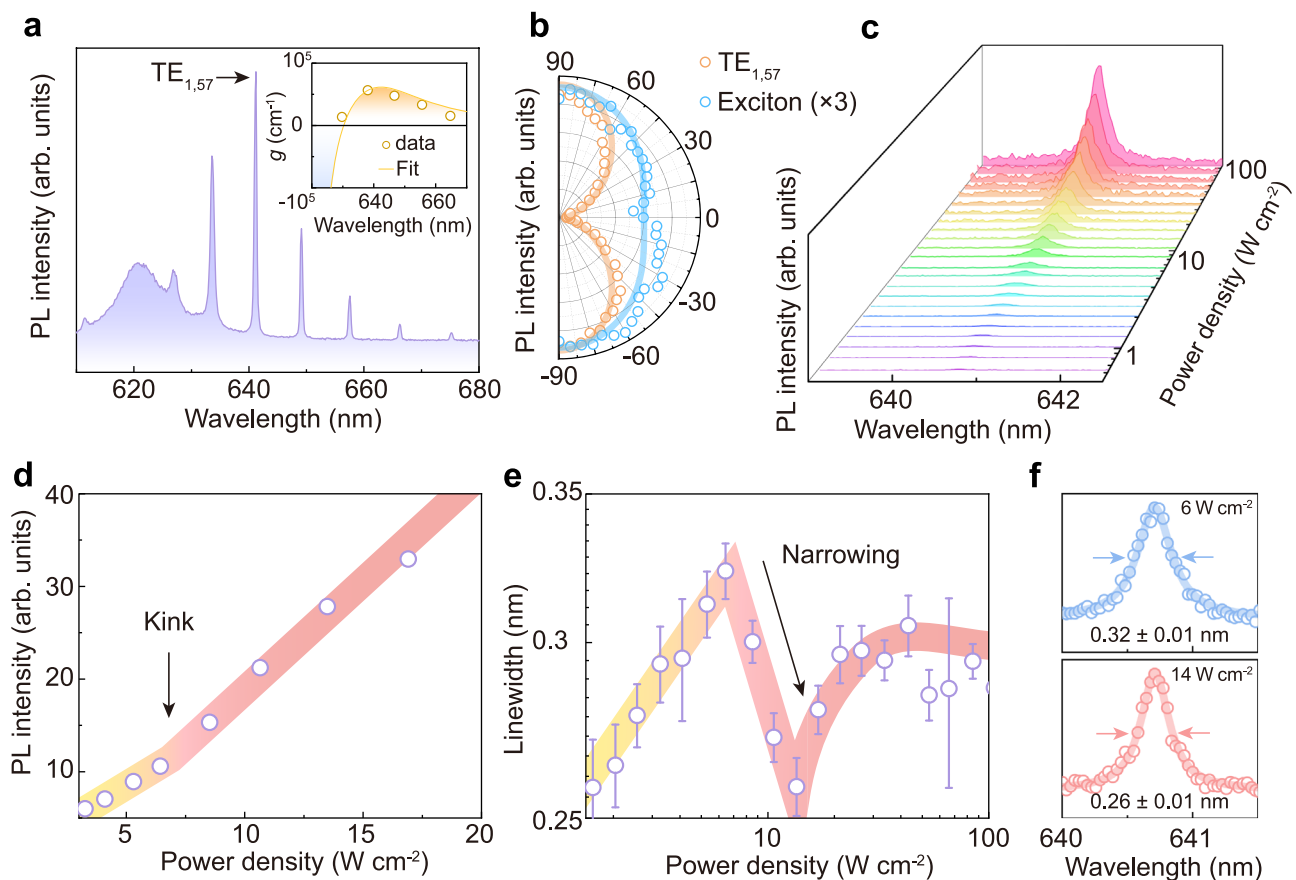


Fig. 2 | Spectral characteristics of vdW CLS. **a** PL spectrum of cavity with $d = 500$ nm, $h = 200$ nm, and $h_o = 1000$ nm under 1000 W cm^{-2} pumping. Inset is gain coefficient g spectrum of cavity-embedded WS₂. **b** Polarization of TE_{1,57} mode and exciton peak in (a). **c** High-resolution PL spectra of TE_{1,57} under various pump

power densities. **d** Light-light curve. **e** Linewidth narrowing under various pump power densities. The error bars represent the deviations from bi-Lorentzian fittings. **f** Lorentzian fits of TE_{1,57} below and above threshold.

temperature. The PL spectrum in Fig. 1f exhibits multiple sharp peaks coexisting with excitonic resonances characteristic of the WS₂ monolayer. The narrow resonances correspond to cavity modes, which can be categorized as first- and second-order TE modes (TE₁ and TE₂, respectively). The full-width at half maximum (FWHM) of the TE resonances indicates an optical gain⁴⁰, which is characteristic of the cavity-embedded WS₂ monolayer⁴⁰. The gain spectrum shows a strong excitonic enhancement of $\sim 5 \times 10^4 \text{ cm}^{-1}$ at about 640 nm at room temperature, as illustrated in the inset of Fig. 2a (see Methods and Supplementary Fig. S4). This excitonic gain in our structure is comparable to the recently reported trionic gain in bilayer MoTe₂¹⁷, confirming the potential of 2D excitons to act as gain sources for CLSs. Excellent stability and reproducibility were achieved in different samples, indicating robust device performances of our vdW CLS architecture (Supplementary Fig. S6).

The design of the cavity mode can be optimized to maximize the optical gain in the energy range of excitons in a WS₂ monolayer at $\sim 640 \text{ nm}$. Furthermore, TE₂ modes are cut-off by a reduced 500 nm ring width to simplify the cavity characterization and reduce the mode competition. The PL spectrum of such an optimized cavity is shown in Fig. 2a. A high-intensity TE₁ mode was observed, exhibiting the maximum gain at 640.7 nm. Our simulation identified this mode as TE_{1,57}, where 57 denotes the azimuthal number m ⁴⁰. A linear polarization degree of as high as 94% was observed for the TE_{1,57} mode (Fig. 2b) in a geometry where the light was collected from a spot with 1 μm diameter at the perimeter of the ring (see Methods and Supplementary Fig. S5). The behavior of TE_{1,57} mode was

monitored under variations of the excitation power density by more than two orders of magnitude in the range between 0.6 to 200 W cm^{-2} , as shown in Fig. 2c.

At low excitation powers, the TE_{1,57} mode was weakly resolved in the spectrum (Fig. 2d). The dependence of its intensity on the excitation power demonstrated a $(60 \pm 5)\%$ change in the slope at 10 W cm^{-2} . At the same power threshold, the FWHM of the TE_{1,57} reversed its increasing trend, reaching a minimum of $(0.26 \pm 0.01) \text{ nm}$ at 14 W cm^{-2} (Fig. 2e, f). Consequently, the total quality factor, defined as $Q = \lambda/\text{FWHM}$, changed abruptly from 2000 to 2500, demonstrating a rising gain in the cavity mode⁴⁰. The observed power-dependent nonlinearities constitute the preliminary evidence of the modification of the emissive characteristics of our structure at a threshold power of 10 W cm^{-2} .

Temporal coherence studies

We further verified the nature of the coherence transition by exploring power-dependent measurements of the second-order photon correlation functions $g^{(2)}(t)$. For these experiments, we selected the TE_{1,57} mode because of its strong intensity, near unity degree of linear polarization and narrow FWHM of $\sim 0.3 \text{ nm}$. The correlation $g^{(2)}(t)$ measurements were conducted in the standard Hanbury Brown and Twiss (HBT) setup, which is schematically displayed in Fig. 3a. In our cavity-WS₂ system, the cavity interacts with the pumped WS₂ monolayer exhibiting excitonic gain (Fig. 3b), leading to a conversion of photon statistics from chaotic to coherent with an increased pumping

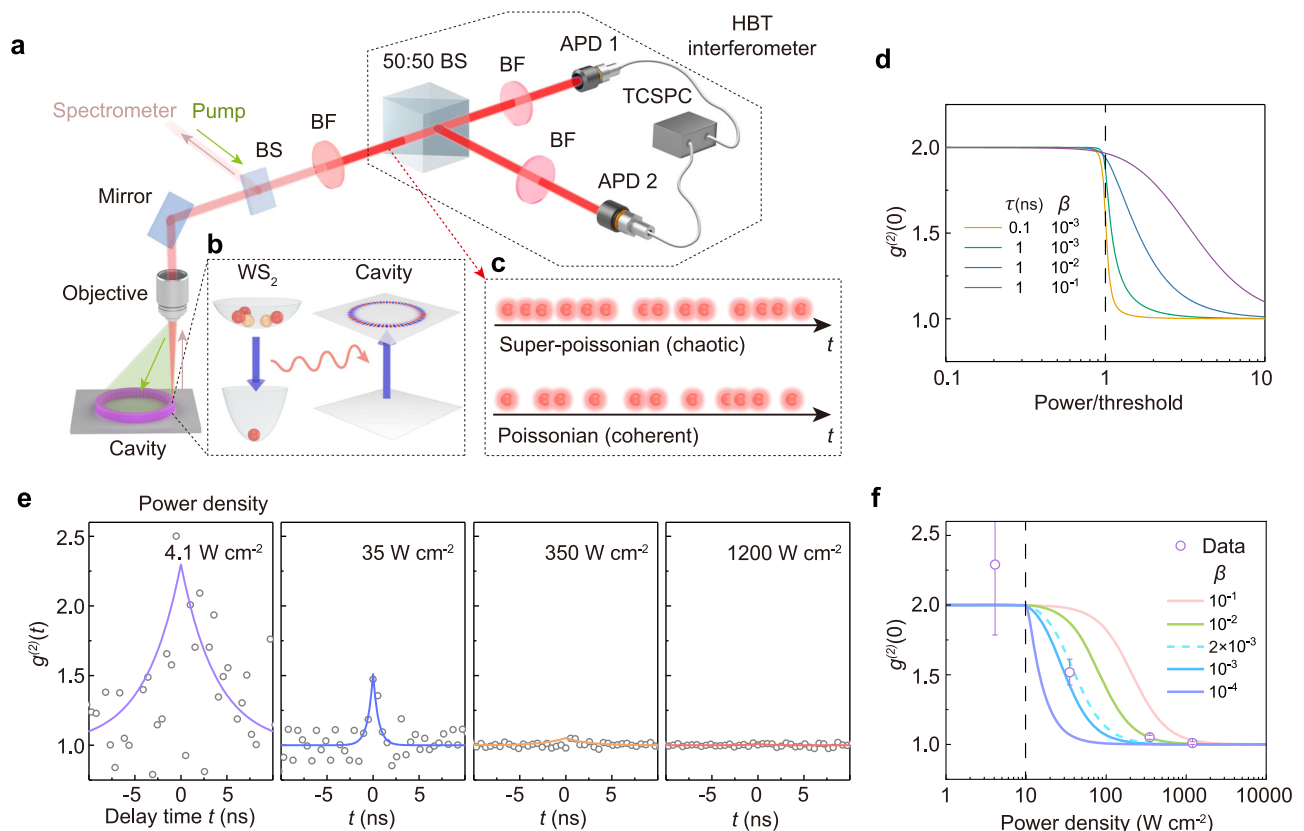


Fig. 3 | Temporal coherence of vdW CLS. **a** Schematic of second-order correlation function $g^{(2)}(t)$ measurement. Cavity emission through the bandpass filters (BFs) is split into two channels by a 50:50 beam splitter (BS) guided to two avalanche photodiodes (APDs) for time-correlated single photon counting (TCSPC). **b** Sketch of coupling between cavity WGMs and WS₂ exciton and trion. **c** Sketches of different types of light statistics measured by $g^{(2)}(t)$. **d** Theoretical analysis of power

dependent $g^{(2)}(0)$ for the cavities with various emitter lifetime τ and spontaneous emission coupling factor β . The cavity-related photon lifetime τ_{ph} is fixed at 0.01 ns. **e** Second-order correlation function $g^{(2)}(t)$ under different pump power densities. **f** Coherence transition of $g^{(2)}(0)$ as a function of pump power density. Solid and dashed lines are from the theoretical model with a fixed coherence threshold of 10 W cm^{-2} . The error bars represent the deviations from fittings.

(Fig. 3c), while the equal-time function $g^{(2)}(0)$ drops from 2 to 1 as the conversion takes place (Fig. 3d).

The experimental $g^{(2)}(t)$ functions of the TE_{1,57} mode, isolated spectrally using band-pass filters under various pump power densities, are demonstrated in Fig. 3e. Below the threshold, we found that $g^{(2)}(0)$ was larger than 1, indicating the super-Poissonian distribution of the emitted photons, a spontaneous emission characteristic of the classical light. Above the threshold, we observed a gradual decrease of $g^{(2)}(0)$ until the value of $g^{(2)}(0) = 1.06 \pm 0.06$, which signifies the transition towards a Poissonian distribution of the photons and the realization of a coherent regime. Our characterization of the TE_{1,57} mode demonstrated direct evidence of coherence.

The chaotic-to-coherence conversion in our vdW cavity was found to be unusual in its gradual and soft acquisition of coherence (Fig. 3f), unlike a rapid change observed for lasers constructed from conventional bulk gain media⁴⁶. To understand the unique characteristics of the vdW CLS with a monolayer optical gain medium, we conducted a theoretical analysis of the photon statistics based on the rate equation model considering the recombination dynamics of neutral excitons, charge excitons (trions), and biexcitons in the presence of cavity coupling (Supplementary Note 7). The model predicts the evolution of the $g^{(2)}(0)$ value with varied pump power as a function of two critical

parameters: the emitter lifetime τ and cavity coupling constant β , as illustrated in Fig. 3d. Under the same cavity condition with photon lifetime τ_{ph} , increased τ or β can convert the stiff transition of $g^{(2)}(0)$ from 2 to 1 into a relatively gradual falling at the coherence threshold. $g^{(2)}(0)$ at the threshold is approximately expressed by the ratio of photon and emitter lifetimes τ_{ph}/τ and coupling ratio β as (Supplementary Note 7):

$$g_{thr}^{(2)}(0) \approx \frac{3\tau_{ph}/\tau + \sqrt{\beta}(5\tau_{ph}/\tau + 4)}{2\tau_{ph}/\tau + \sqrt{\beta}(4\tau_{ph}/\tau + 2)} \quad (1)$$

At a high Q system with the emitter lifetime much longer than photon lifetime ($\tau_{ph}/\tau \ll 1$), $g^{(2)}(0)$ at the threshold reaches 1.5 with small β , and approximates to 2 when β approaches 1. This theory indicates that high coupling strength (measured by β) and strong optical confinement (evaluated by Q) both favor reducing coherence for 2D excitons even if the threshold is reached.

Employing this theoretical model, we obtained the fit to the experimental data with a total emitter lifetime τ_{tot} of 1.81 ns after considering the contributions from excitons, trions, and biexcitons of monolayer WS₂⁴⁷ (Supplementary Note 7). The best fit results in $\beta = 0.002$, as illustrated in Fig. 3f. These results indicate that the soft coherence threshold originates from a relatively high cavity coupling

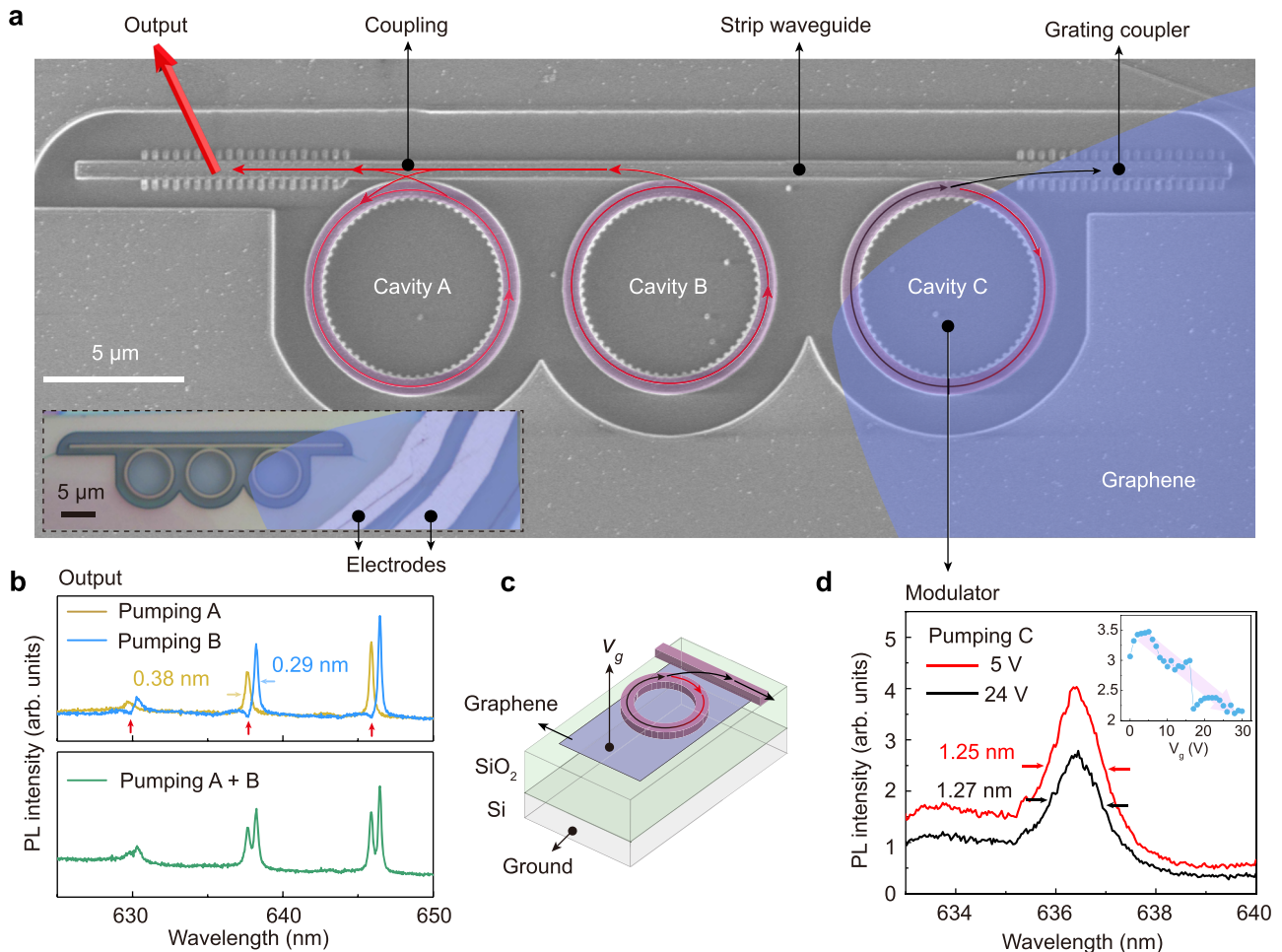


Fig. 4 | Proof-of-concept on-chip vdW PIC. **a** SEM image of PIC consisted of three ring CLSs, a stripe waveguide, a graphene modulator, and two grating couplers at waveguide ends. Heterostructures assembled with monolayer WS₂ are shaded with purple colour, while those with monolayer graphene are shaded with blue. Inset is the optical micro-image of PIC showing Cr/Au electrodes connected to the graphene modulator. **b** Emission spectra measured at the grating coupler by optically

pumping CLSs A and B separately and simultaneously under a pump power density of 1000 W cm⁻². Red arrows denote the dips caused by intercoupling between CLSs A and B. **c** Schematic of the graphene modulator with silicon back gate. **d** TE_{1,57} spectra of C under different gate voltages V_g with inset of mode intensity modulated by the gate voltage.

constant β with respect to the emitter lifetime τ of exciton complexes in the high-quality cavity. This finding underscores the difference in the characteristics of the coherence threshold between our vdW CLSs and conventional lasers based on bulk gain media with electron-hole plasma gain⁴⁶, whose β and τ are a few orders lower than our CLS.

Van der Waals photonic integrated circuit

Based on the monolithic architecture of our vdW CLS, we fabricated a prototype PIC entirely assembled in a vdW heterostructure, consisting of three vdW ring cavities coupled to an hBN waveguide equipped with free-beam grating couplers, all within the same silicon chip. Additionally, one of the cavities was electrically controllable with a graphene modulator. The scanning electron microscopy image of the PIC is shown in Fig. 4a. In this PIC, the waveguide was fabricated by patterning a 200 nm thick hBN into a stripe with planar dimensions of $40 \times 0.5 \mu\text{m}$. This waveguide evanescently coupled light emitted from the three ring CLSs, labeled as A, B, and C in Fig. 4a. The CLSs were made to be distinguishable in resonances by finely tuning the radii of the rings by -10 nm, ensuring all the $\text{TE}_{1,57}$ mode resonances studied here fall within the gain spectrum from 635 nm to 650 nm range. The evanescent coupling was determined by the gap between the cavity and waveguide. The cavity emission was guided by the waveguide to free-beam grating couplers. Example emission spectra collected from this coupler when optically pumping A and B separately or concurrently are presented in Fig. 4b. These results demonstrate that our design enabled selective or concurrent excitation of different CLSs and that multiple CLSs can be coupled to the same waveguide. The propagation length of the waveguide is estimated to be a millimetre long (Supplementary Note 6), demonstrating that our vdW PICs can be extended to chip-scale integration with ultralow losses, as required for viable device applications.

In the PL emission spectrum of CLS B measured at the free-beam grating coupler, the $\text{TE}_{1,57}$ mode at 638 nm demonstrated a narrow linewidth of 0.29 nm, corresponding to a Q factor of 2200. This high Q was comparable to the cavity without waveguide coupling, indicating that the coupling through the gap of 100 nm between the cavity and the waveguide was nearly lossless. Note that since the waveguide-coupled CLSs do not incur any additional losses compared to those without waveguide coupling studied in the above discussion, and both cases share an almost identical cavity structure (differing only around 10 nm in radius fine-tuning), as well as the same material assembly, the CLSs presented in Fig. 4 are considered to exhibit the same coherence examined in the sample whose data are presented in Fig. 3. We also notice the absorptive features in the emission spectrum of CLS B, as denoted by red arrows in the top panel of Fig. 4b. The absorptive dips correspond to the wavelengths of the CLS A modes, indicating that a portion of the light confined in B and coupled into the waveguide, is subsequently absorbed by A. This inter-cavity coupling confirms our PIC effectively connects all the integrated CLSs.

The final component of our PIC was an electrical modulator of emission intensity integrated into the CLS C in the form of an underlying graphene monolayer connected with electrodes consisted of Cr and Au. The modulator was constructed as a field effect transistor structure with a silicon back gate, as illustrated in Fig. 4c. The application of the gate voltage V_g enabled tunability of the Fermi level in graphene. The impact of the electrical modulation was tested by optically pumping C and detecting the emission spectra at the grating coupler. The modification of the emission spectra by V_g is shown in Fig. 4d. The variation of V_g from 5 V to 24 V led to the $\text{TE}_{1,57}$ mode broadening by 2%, resulting in the total emission intensity quenching by 40%. The electrical modulation of $\text{TE}_{1,57}$ mode is related to the modified screening from the graphene layer, which alters the energy of excitons in monolayer TMD⁴⁸, leading to the quenched emission intensity. Our vdW architecture creates prospects to develop infrared CLSs using, e.g., interlayer excitons³⁴ or narrow band gap systems akin to bilayer graphene as the optical gain media⁴⁹.

Discussion

In this work, we have introduced the concept of a vdW PIC. Our monolithic vdW PIC architecture addresses key fabrication challenges, delivering unprecedented performance, including low pump power thresholds, high efficiency and miniaturized integration. Unlike current technologies based on 2D materials, our vdW PIC can generate, propagate, couple, and modulate coherent light on a single silicon chip. Moreover, our design could enable low-cost, large-scale, and efficient integration of diverse photonic devices, with straightforward implementation of electro-optic interconnections. Our results represent a major step toward the practical application of 2D materials, paving the way for the large-scale integration of vdW photonics using standard silicon manufacturing processes.

Methods

Gain coefficient

The gain coefficient g is derived for the gain media of monolayer WS_2 in a cavity with an intrinsic Q factor Q_{int} expressed as⁴⁰.

$$g = -\frac{2\pi n_r}{\lambda F} \left(\frac{\text{FWHM}}{\lambda} - \frac{1}{Q_{\text{int}}} \right) \quad (2)$$

Here, Q_{int} quantifies the cavity confinement in the absence of the gain medium of monolayer WS_2 , though its value may account for additional absorptive contributions, such as the Si substrate. By incorporating Si absorption into the analysis and applying Eq. 2, the gain intensity of WS_2 is obtained by employing the FWHM of WGMs at different resonant wavelengths. We found g is positive at 630 to 660 nm and reaches a maximum at 640 nm. This Si absorption can be reduced to trivial by increasing the SiO_2 thickness h_o to 1000 nm.

Device fabrication

First, a monolayer WS_2 was mechanically exfoliated and dry-transferred to be sandwiched between two hBN flakes. Subsequently, the heterostructure was patterned to the ring cavity by electron beam lithography and reactive ion etching on the Si substrate covered by SiO_2 following standard silicon manufacture processes. The PIC was fabricated using the same process. The cavities in PIC were fabricated at the location where the WS_2 covers, and passive devices do not require WS_2 coverage. Finally, the graphene is connected to an electrode of 5 nm Cr followed by 50 nm Au deposited by an electron beam evaporator.

Laser characterization

The laser was mounted on a scanning stage under the confocal micro-PL system. A $20 \times$ objective lens (NA of 0.4) was used for focusing the pump laser and receiving the cavity emission. The pump laser has a spot size of approximately $7 \mu\text{m}$, ensuring excitation coverage across the entire cavity. Gratings at the ring edge facilitate the reception of a portion of cavity emission in the vertical direction. Due to the confocal operation of our setup, cavity emission only from an area as small as $1 \mu\text{m}$ can be detected, and we adjusted the detection region to be at the ring in order to maximize the signal intensity. The power density was varied for the power-dependent measurement, and the cavity emission was collected by the confocal system and sent to a spectrometer equipped with a charge-coupled device detector. All the measurements are conducted at room temperature and in an ambient environment.

Power-dependent PL of $\text{TE}_{1,57}$ of the same ring cavity was conducted for the pumping range from 0.6 to 200 W cm^{-2} . The background noise is minimized by integrating PL with exposure time as long as 200 s, above which the signal-to-noise ratio is not improved.

For the second-order correlation measurement, the sample emission spectrally filtered by the spectrometer was sent to a

Hanbury–Brown and Twiss set-up consisting of a 50:50 beamsplitter with two Si single-photon avalanche photodiodes and a time-correlated single-photon counter. The entire system had a timing resolution of 0.15 ns, limited by the photodetectors.

Data availability

We declare that the data supporting the findings of this study are available within the paper.

References

- Liu, Y. et al. A fully hybrid integrated erbium-based laser. *Nat. Photonics* **18**, 829–835 (2024).
- Yang, J. et al. Titanium:sapphire-on-insulator integrated lasers and amplifiers. *Nature* **630**, 853–859 (2024).
- Tran, M. A. et al. Extending the spectrum of fully integrated photonics to submicrometre wavelengths. *Nature* **610**, 54–60 (2022).
- Ma, R.-M. & Oulton, R. F. Applications of nanolasers. *Nat. Nanotechnol.* **14**, 12–22 (2019).
- Liu, Y. et al. Integrated vortex soliton microcombs. *Nat. Photonics* **18**, 632–637 (2024).
- Atabaki, A. H. et al. Integrating photonics with silicon nanoelectronics for the next generation of systems on a chip. *Nature* **556**, 349–354 (2018).
- Shen, Y. et al. Deep learning with coherent nanophotonic circuits. *Nat. Photonics* **11**, 441–446 (2017).
- Fang, A. W. et al. Electrically pumped hybrid AlGaInAs-silicon evanescent laser. *Opt. Express* **14**, 9203 (2006).
- Zhang, J. et al. III-V-on-Si photonic integrated circuits realized using micro-transfer-printing. *APL Photonics* **4**, 110803 (2019).
- Park, J. S., Tang, M., Chen, S. & Liu, H. Heteroepitaxial growth of iii-v semiconductors on silicon. *Crystals* **10**, 1–36 (2020).
- Margetis, J. et al. Si-Based GeSn Lasers with Wavelength Coverage of 2–3 μm and Operating Temperatures up to 180 K. *ACS Photonics* **5**, 827–833 (2018).
- Splendiani, A. et al. Emerging photoluminescence in monolayer MoS₂. *Nano Lett.* **10**, 1271–1275 (2010).
- Mak, K. F., Lee, C., Hone, J., Shan, J. & Heinz, T. F. Atomically thin MoS₂: A new direct-gap semiconductor. *Phys. Rev. Lett.* **105**, 136805 (2010).
- He, K. et al. Tightly bound excitons in monolayer WSe₂. *Phys. Rev. Lett.* **113**, 026803 (2014).
- Mak, K. F. et al. Tightly bound trions in monolayer MoS₂. *Nat. Mater.* **12**, 207–211 (2012).
- del Águila, A. G. et al. Ultrafast exciton fluid flow in an atomically thin MoS₂ semiconductor. *Nat. Nanotechnol.* **18**, 1012–1019 (2023).
- Wang, Z. et al. Excitonic complexes and optical gain in two-dimensional molybdenum ditelluride well below the Mott transition. *Light Sci. Appl.* **9**, 39 (2020).
- Geim, A. K. & Grigorieva, I. V. Van der Waals heterostructures. *Nature* **499**, 419–425 (2013).
- Ren, T. & Loh, K. P. On-chip integrated photonic circuits based on two-dimensional materials and hexagonal boron nitride as the optical confinement layer. *J. Appl. Phys.* **125**, 230901 (2019).
- Wu, S. et al. Monolayer semiconductor nanocavity lasers with ultralow thresholds. *Nature* **520**, 69–72 (2015).
- Ye, Y. et al. Monolayer excitonic laser. *Nat. Photonics* **9**, 733–737 (2015).
- Salehzadeh, O. et al. Optically pumped two-dimensional MoS₂ lasers operating at room-temperature. *Nano Lett.* **15**, 5302–5306 (2015).
- Liu, Y. et al. Room temperature nanocavity laser with interlayer excitons in 2D heterostructures. *Sci. Adv.* **5**, eaav4506 (2019).
- Paik, E. Y. et al. Interlayer exciton laser of extended spatial coherence in atomically thin heterostructures. *Nature* **576**, 80–84 (2019).
- Sung, J. et al. Room-temperature continuous-wave indirect-bandgap transition lasing in an ultra-thin WS₂ disk. *Nat. Photonics* **16**, 792–797 (2022).
- Li, Y. et al. Room-temperature continuous-wave lasing from monolayer molybdenum ditelluride integrated with a silicon nanobeam cavity. *Nat. Nanotechnol.* **12**, 987–992 (2017).
- Zhao, L. et al. High-Temperature Continuous-Wave Pumped Lasing from Large-Area Monolayer Semiconductors Grown by Chemical Vapor Deposition. *ACS Nano* **12**, 9390–9396 (2018).
- Lin, Z. et al. Defect engineering of two-dimensional transition metal dichalcogenides. *2D Mater.* **3**, 022002 (2016).
- Ahn, K. et al. Impact of intrinsic atomic defects on the electronic structure of MoS₂ monolayers. *Nanotechnology* **25**, 375703 (2014).
- Wei, G., Stanev, T. K., Czaplowski, D. A., Jung, I. W. & Stern, N. P. Silicon-nitride photonic circuits interfaced with monolayer MoS₂. *Appl. Phys. Lett.* **107**, 091112 (2015).
- Wang, J. et al. Dual-coupling-guided epitaxial growth of wafer-scale single-crystal WS₂ monolayer on vicinal a-plane sapphire. *Nat. Nanotechnol.* **17**, 33–38 (2022).
- Chubarov, M. et al. Wafer-Scale Epitaxial Growth of Unidirectional WS₂ Monolayers on Sapphire. *ACS Nano* **15**, 2532–2541 (2021).
- Jang, A. R. et al. Wafer-Scale and Wrinkle-Free Epitaxial Growth of Single-Oriented Multilayer Hexagonal Boron Nitride on Sapphire. *Nano Lett.* **16**, 3360–3366 (2016).
- Lee, J. S. et al. Wafer-scale single-crystal hexagonal boron nitride film via self-collimated grain formation. *Science* **362**, 817–821 (2018).
- Ren, T., Song, P., Chen, J. & Loh, K. P. Whisper Gallery Modes in Monolayer Tungsten Disulfide-Hexagonal Boron Nitride Optical Cavity. *ACS Photonics* **5**, 353–358 (2018).
- Khelifa, R. et al. Coupling Interlayer Excitons to Whispering Gallery Modes in van der Waals Heterostructures. *Nano Lett.* **20**, 6155–6161 (2020).
- Lee, S. Y., Jeong, T. Y., Jung, S. & Yee, K. J. Refractive Index Dispersion of Hexagonal Boron Nitride in the Visible and Near-Infrared. *Phys. status solidi* **256**, 1800417 (2019).
- Fröch, J. E., Hwang, Y., Kim, S., Aharonovich, I. & Toth, M. Photonic Nanostructures from Hexagonal Boron Nitride. *Adv. Opt. Mater.* **7**, 1801344 (2019).
- Kim, S. et al. Photonic crystal cavities from hexagonal boron nitride. *Nat. Commun.* **9**, 2623 (2018).
- Ren, T. et al. Optical Gain Spectrum and Confinement Factor of a Monolayer Semiconductor in an Ultrahigh-Quality Cavity. *Nano Lett.* **23**, 11601–11607 (2023).
- Magorrian, S. J. et al. Band alignment and interlayer hybridisation in transition metal dichalcogenide/hexagonal boron nitride heterostructures. *2D Mater.* **9**, 045036 (2022).
- Sanchez, D. A., Dai, Z. & Lu, N. 2D Material Bubbles: Fabrication, Characterization, and Applications. *Trends Chem.* **3**, 204–217 (2021).
- Holler, J. et al. Air tightness of hBN encapsulation and its impact on Raman spectroscopy of van der Waals materials. *2D Mater.* **7**, 015012 (2019).
- Jung, J. et al. Defect Passivation of 2D Semiconductors by Fixating Chemisorbed Oxygen Molecules via h-BN Encapsulations. *Adv. Sci.* **11**, 2310197 (2024).
- Kretinin, A. V. et al. Electronic properties of graphene encapsulated with different two-dimensional atomic crystals. *Nano Lett.* **14**, 3270–3276 (2014).
- Pan, S. H., Deka, S. S., El Amili, A., Gu, Q. & Fainman, Y. Nanolasers: Second-order intensity correlation, direct modulation and electromagnetic isolation in array architectures. *Prog. Quantum Electron.* **59**, 1–18 (2018).

47. Lien, D.-H. et al. Electrical suppression of all nonradiative recombination pathways in monolayer semiconductors. *Science* **364**, 468–471 (2019).
48. Tebbe, D. et al. Tailoring the dielectric screening in WS₂-graphene heterostructures. *npj 2D Mater. Appl.* **7**, 1–7 (2023).
49. Zhang, Y. et al. Direct observation of a widely tunable bandgap in bilayer graphene. *Nature* **459**, 820–823 (2009).

Acknowledgements

H.S. acknowledges the support from the University of Macau (CPG2025-00034-IAPME and SRG2023-00025), and the Science and Technology Development Fund (FDCT), Macao SAR (0122/2023/RIA2). A.G.D.A. acknowledges the support from the Ramón y Cajal Fellowship program, awarded by the Ministry of Science, Innovation, and Universities of Spain (RYC2022-037107-I, MINECO, Spain). K.W. and T.T. acknowledge support from the JSPS KAKENHI (21H05233 and 23H02052) and World Premier International Research Center Initiative (WPI), MEXT, Japan. K.S.N. acknowledges support from the Ministry of Education, Singapore (EDUNC-33-18-279-V12, Research Centre of Excellence award to the Institute for Functional Intelligent Materials (I-FIM)) and the Royal Society (RSRP\R\190000, UK). M.K. acknowledges support from the Ministry of Education, Singapore (MOE-T2EP50122-0012), and the Air Force Office of Scientific Research and the Office of Naval Research Global (FA8655-21-1-7026).

Author contributions

H.S. and T.R. conceptualized and designed the study. T.R., A.G.D.A., and Z.C. performed all data analysis and visualization. T.R. and X.G. fabricated the sample structures. T.R., A.G.D.A., Z.C., X.Z., R.D., and M.G. conducted optical experiments, data collection, and result discussion. T.R. and Q.X. developed the theoretical model. K.W. and T.T. grew hBN crystals. H.S. supervised the research conducted at the University of Macau. K.S.N. and M.K. supervised the experiments conducted at the National University of Singapore. T.R., A.G.D.A., and Z.C. wrote the original draft. K.S.N., M.K., and H.S. reviewed and edited the final manuscript.

Competing interests

The authors declare no competing interests.

Additional information

Supplementary information The online version contains supplementary material available at <https://doi.org/10.1038/s41467-025-60778-2>.

Correspondence and requests for materials should be addressed to Andrés. Granados del Águila, Kostya S. Novoselov, Maciej Koperski or Handong Sun.

Peer review information *Nature Communications* thanks Arka Majumdar and the other, anonymous, reviewer(s) for their contribution to the peer review of this work. A peer review file is available.

Reprints and permissions information is available at <http://www.nature.com/reprints>

Publisher's note Springer Nature remains neutral with regard to jurisdictional claims in published maps and institutional affiliations.

Open Access This article is licensed under a Creative Commons Attribution-NonCommercial-NoDerivatives 4.0 International License, which permits any non-commercial use, sharing, distribution and reproduction in any medium or format, as long as you give appropriate credit to the original author(s) and the source, provide a link to the Creative Commons licence, and indicate if you modified the licensed material. You do not have permission under this licence to share adapted material derived from this article or parts of it. The images or other third party material in this article are included in the article's Creative Commons licence, unless indicated otherwise in a credit line to the material. If material is not included in the article's Creative Commons licence and your intended use is not permitted by statutory regulation or exceeds the permitted use, you will need to obtain permission directly from the copyright holder. To view a copy of this licence, visit <http://creativecommons.org/licenses/by-nc-nd/4.0/>.

© The Author(s) 2025